Inorganic Chemistry

Article

pubs.acs.org/IC

Electronic Effects of Ligand Substitution on Spin Crossover in a Series of Diiminoquinonoid-Bridged Fe^{II}_2 Complexes

Jesse G. Park,[†] Ie-Rang Jeon,[†] and T. David Harris*

Department of Chemistry, Northwestern University, Evanston, Illinois 60208-3113, United States

Supporting Information

ABSTRACT: A series of four isostructural Fe^{II}_2 complexes, $[(TPyA)_2Fe_2(^{X}L)]^{2+}$ (TPyA = tris(2-pyridylmethyl)amine; $^{X}L^{2-}$ = doubly deprotonated form of 3,6-disubstituted-2,5-dianilino-1,4-benzoquinone; X = H, Br, Cl, and F), were synthesized to enable a systematic study of electronic effects on spin crossover behavior. Comparison of X-ray diffraction data for these complexes reveals the sole presence of high-spin Fe^{II} at 225 K and mixtures of high-spin and low-spin Fe^{II} at 100 K, which is indicative of incomplete spin crossover. In addition, crystal packing diagrams show that these complexes are well-isolated from one another in the solid state, owing primarily to the presence of bulky tetra(aryl)borate counteranions, such that spin crossover is likely not significantly affected by intermolecular interactions. Variable-temperature dc magnetic susceptibility data confirm the structural observations and reveal that 54(1), 56(1), 62(1), and 84(1)% of Fe^{II} centers remain high-spin even below 65 K. Moreover, fits to magnetic data provide crossover temperatures of $T_{1/2}$ = 160(1), 124(1), 121(1), and 110(1) K for X = H, Br, Cl, and F, respectively, along with enthalpies of ΔH = 11.4(3), 8.5(3), 8.3(3), and 7.5(2) kJ/mol, respectively. These parameters decrease with increasing electronegativity of X and thus increasing electron-withdrawing character of $^{X}L^{2-}$, suggesting that the observed trends originate primarily from inductive effects of X. Moreover, when plotted as a function of the Pauling electronegativity of X, both $T_{1/2}$ and ΔH undergo a linear decrease. Further analyses of the low-temperature magnetic data and variable-temperature Mössbauer spectroscopy suggest that the incomplete spin crossover behavior in $[(TPyA)_2Fe_2(^{X}L)]^{2+}$ is best described as a transition from purely $[Fe_{HS}\text{-}Fe_{HS}]$ (HS = high-spin) complexes at high temperature to a mixture of $[Fe_{HS}\text{-}Fe_{HS}]$ and $[Fe_{HS}\text{-}Fe_{LS}]$ (LS = low-spin) complexes at low temperature, with the number of $[Fe_{HS}\text{-}Fe_{HS}]$ species increasing with decreasing electron-withdrawing character of $^{X}L^{2-}$.

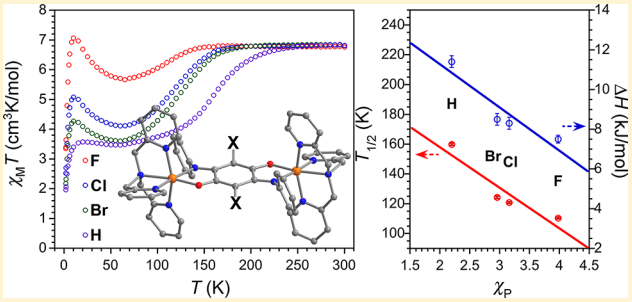

INTRODUCTION

Complexes that undergo a transition in electronic configuration from a low-spin to a high-spin state as a function of an external stimulus, such as temperature, light, or pressure, constitute a class of molecules known as spin crossover complexes.[1] These species have garnered tremendous interest over several decades, largely owing to their potential application as active components in molecular memories, displays, and sensors.[2−5] The spin crossover phenomenon is most commonly observed in pseudo-octahedral Fe^{II} complexes that feature an Fe coordination environment comprised by six nitrogen donor atoms. This metal−ligand combination can give rise to a situation in which the ligand field splitting energy is comparable in magnitude to the spin pairing energy.[6,7] In this case, increasing temperature results in an entropy-driven conversion from a low-spin S = 0 ground state to a high-spin S = 2 excited state, which is accompanied by corresponding changes in structural, magnetic, and spectroscopic properties.

The realization of applications associated with thermally induced spin crossover requires the ability to adjust the crossover temperature ($T_{1/2}$), defined as the temperature at which the low-spin state and the high-spin state are equally populated. As such, predicting and controlling $T_{1/2}$ at the molecular level by judicious modulation of ligand field represents an important synthetic chemistry challenge. Toward this end, an ideal system for studying the effects of ligand field on spin crossover might involve a series of complexes that feature a common local metal coordination environment and systematic variation of the ligand substitution pattern. Complicating such studies, spin crossover in a bulk sample is also largely governed by solid-state packing effects in which elastic interactions between molecular species significantly influence the crossover.[8,9] As such, changes in steric and packing effects associated with changes in a substituent should be minimized in order to extract a meaningful correlation between electronic effects and spin crossover. To date, only a few systematic studies of electronic effects on spin crossover have been reported, most notably those involving substitution of the four-position of an axially coordinated pyridyl ligand in six-coordinate Fe^{II} complexes.[10−12] Here, incorporation of electron-withdrawing substituents led to increased π-back-bonding character of the pyridyl ligands, thereby stabilizing the low-spin state and increasing $T_{1/2}$. In addition, a recent report

Received: October 24, 2014
Published: December 12, 2014

   dx.doi.org/10.1021/ic5025586 | Inorg. Chem. 2015, 54, 359−369

studied the variation of electronic and steric effects across a series of four-coordinate pseudotetrahedral Fe^{II} complexes supported by a strongly donating tris(carbene)borate ligand.[13]

Along with the extensive library of mononuclear Fe^{II} complexes that exhibit thermally induced spin crossover, a number of dinuclear Fe^{II}_2 complexes have also been shown to demonstrate this phenomenon.[14−17] In a dinuclear complex, spin crossover often occurs via an intermediate state comprising an equimolar mixture of low-spin and high-spin Fe^{II} centers, which can be made up of either a localized mixed-spin state [Fe_{HS}-Fe_{LS}] (HS = high-spin, LS = low-spin) or a 1:1 mixture of pure [Fe_{HS}-Fe_{HS}] and [Fe_{LS}-Fe_{LS}] states. Density functional theory (DFT) calculations have suggested that the exact nature of spin crossover in these complexes depends on the relative enthalpies of these three possible compositions, which determine whether the transition will follow one-step, two-step, or incomplete spin crossover.[18] In addition, the extent of stabilization of the intermediate state is largely governed by the ability of the Fe coordination sphere to distort from idealized coordination geometries in order to undergo the spin crossover. Here, highly rigid or already distorted coordination environments act to disfavor full conversion to low-spin Fe^{II} with decreasing temperature, thus often giving rise to incomplete spin crossover behavior.[17,19]

Derivatives of 2,5-dihydroxy-1,4-benzoquinone have long been employed as bridging ligands between two metal centers.[20,21] Indeed, scores of dinuclear molecular complexes and extended solids containing both diamagnetic and paramagnetic derivatives of 2,5-dihydroxy-1,4-benzoquinone as bridging ligands have been reported and thoroughly investigated.[22−26] Among these, Fe^{II}_2 complexes bridged by 3,6-dihydroxy- and 3,6-bis(*tert*-butyl)-2,5-dihydroxy-1,4-benzoquinone have been shown to exhibit thermally induced spin crossover.[26] However, relative differences in the crystal structures of these complexes precluded the correlation of ligand substitution effects on spin crossover.

The observation of spin crossover in these Fe^{II}_2 complexes, in conjunction with the dearth of studies that probe electronic effects on spin crossover, prompted us to investigate how the substitution pattern of benzoquinonoid-bridging ligands affects spin crossover in Fe^{II}_2 complexes. Toward this end, we have targeted the synthesis of Fe^{II}_2 complexes containing 3,6-disubstituted-2,5-dianilino-1,4-benzoquinone derivatives as bridging ligands. Replacement of the hydroxy groups with aniline groups provides steric bulk to minimize intermolecular interactions. Herein, we report the synthesis and characterization of a series of $[(TPyA)_2Fe_2(^{X}L)]^{2+}$ complexes, where $^{X}L^{2-}$ = dianion of 3,6-disubstituted-2,5-dianilino-1,4-benzoquinone and X = H, Br, Cl, and F. The isostructural nature of these complexes, along with large intermolecular separation in the solid state afforded by aniline groups and tetra(aryl)borate counterions, enables a systemic examination of the electronic effects of ligand substitution on spin crossover using an extensive array of structural, magnetic, and Mössbauer spectroscopic analyses.

EXPERIMENTAL SECTION

General Considerations. Unless otherwise noted, all procedures were performed under a dinitrogen atmosphere using a Vacuum Atmospheres Nexus II glovebox. Glassware was oven-dried at 150 °C for at least 4 h and allowed to cool in an evacuated antechamber prior to use in the glovebox. Acetonitrile (MeCN), diethyl ether (Et_2O), tetrahydrofuran (THF), benzene, and *n*-hexane were dried using a commercial solvent purification system from Pure Process Technology and stored over 3 or 4 Å molecular sieves. Et_2O, THF, benzene, and *n*-hexane were tested with a standard purple solution of sodium benzophenone ketyl in THF to confirm effective oxygen and moisture removal prior to use. Perdeuterated dimethyl sulfoxide (DMSO-d_6) was purchased from Cambridge Isotope Laboratories and stored over 4 Å molecular sieves prior to use. Diatomaceous earth (Celite 545) was purchased from Fisher Scientific and dried by heating at 250 °C under vacuum for 12 h. Sodium tetrafluoroborate was dried at 80 °C under vacuum before use. The compounds tris(2-pyridylmethyl)amine (TPyA)[27] and sodium bis(trimethylsilyl)amide ($Na[N(SiMe_3)_2]$)[28] were synthesized as previously described. The compounds 3,6-dihydro-, 3,6-difluoro-, 3,6-dichloro-, and 3,6-dibromo-2,5-dianilino-1,4-benzoquinone ($^{X}LH_2$; X = H,[29] F,[30] Cl,[31] and Br[31]), sodium tetrakis[3,5-bis(trifluoromethyl)phenyl]borate ($Na(BAr^F)$),[32] Tl(BAr^F),[33] and $Fe(BAr^F)_2$·6MeCN[34] were synthesized through modified literature procedures as described below. All other reagents were obtained from commercial vendors and used without further purification.

2,5-Dianilino-1,4-benzoquinone ($^{H}LH_2$). This compound was synthesized through a modified literature procedure.[29] 1,4-Benzoquinone (1.08 g, 10.0 mmol) was added as a solid to methanol (35 mL) to give a yellow mixture. Aniline (2.23 g, 24.0 mmol) was then added to this suspension, and the resulting dark brown mixture was stirred at room temperature for 12 h. The brown mixture was then filtered, and the brown residue was washed with water (3 × 25 mL) and then dried at 50 °C under vacuum for 12 h to afford 0.637 g (22%) of product as a brown powder. ^{1}H NMR (DMSO-d_6, 500 MHz): δ 9.33 (s, 2H, NH), 7.44 (dd, 2H, aryl-H), 7.38 (dd, 4H, aryl-H), 7.24 (dd, 2H, aryl-H), 5.79 (s, 2H, quinone-H). FT-IR (ATR, cm^{-1}): 3224 (m), 3053 (w), 1636 (w), 1563 (s), 1484 (s), 1441 (s), 1355 (m), 1286 (s), 1230 (m), 1186 (s), 1175 (s), 1079 (w), 1023 (w), 1023 (w), 1000 (w), 913 (w), 894 (w), 857 (w), 840 (m), 759 (m), 739 (s), 724 (s), 690 (s).

2,5-Dianilino-3,6-fluoro-1,4-benzoquinone ($^{F}LH_2$). This compound was synthesized through a modified literature procedure.[30] 2,3,5,6-Tetrafluoro-1,4-benzoquinone (0.108 g, 1.00 mmol) was added as a solid to a solution of sodium acetate (0.150 g, 1.83 mmol) in a mixture of ethanol (10 mL), acetic acid (10 mL), and water (5 mL) to give a purple mixture. Aniline (0.372 g, 4.00 mmol) was then added to this suspension, and the resulting dark brown mixture was heated at 110 °C for 5 h. The dark brown mixture was then filtered while hot, and the dark brown residue was washed with water (3 × 15 mL) and then dried at 50 °C under vacuum for 12 h to afford 0.288 g (88%) of product as a dark brown powder. ^{1}H NMR (DMSO-d_6, 500 MHz): δ 9.16 (s, 2H, NH), 7.34 (dd, 4H, aryl-H), 7.13−7.19 (m, 6H, aryl-H). FTIR (ATR, cm^{-1}): 3240 (m), 3055 (w), 1667 (w), 1594 (m), 1574 (s), 1489 (s), 1440 (s), 1354 (s), 1321 (s), 1305 (m), 1271 (m), 1227 (s), 1176 (m), 1090 (w), 1081 (w), 1064 (w), 1027 (w), 993 (m), 913 (w), 841 (w), 810 (w), 787 (w), 751 (s), 721 (s), 701 (s), 681 (m).

2,5-Dianilino-3,6-dichloro-1,4-benzoquinone ($^{Cl}LH_2$). This compound was synthesized through a modified literature procedure.[31] 2,3,5,6-Tetrachloro-1,4-benzoquinone (2.46 g, 10.0 mmol) was added as a solid to a solution of sodium acetate (0.600 g, 7.32 mmol) in a mixture of ethanol (50 mL), acetic acid (50 mL), and water (25 mL) to give a yellow mixture. Aniline (3.80 g, 40.8 mmol) was then added to this suspension, and the resulting dark brown mixture was heated at 110 °C for 5 h. The dark brown mixture was then filtered while hot, and the dark brown residue was washed with water (3 × 25 mL) and then dried at 50 °C under vacuum for 12 h to afford 1.93 g (82%) of product as a dark brown powder. ^{1}H NMR (DMSO-d_6, 500 MHz): δ 9.64 (s, 2H, NH), 7.33 (dd, 4H, aryl-H), 7.14−7.19 (m, 6H, aryl-H). FTIR (ATR, cm^{-1}): 3232 (m), 3038 (w), 1650 (w), 1602 (w), 1562 (s), 1494 (s), 1480 (s), 1443 (s), 1323 (s), 1309 (s), 1247 (m), 1193 (m), 1167 (w), 1150 (w), 1077 (w), 1025 (m), 1002 (w) 909 (m), 886 (m), 831 (w), 780 (m), 752 (m), 745 (m), 713 (m), 691 (s).

2,5-Dianilino-3,6-dibromo-1,4-benzoquinone ($^{Br}LH_2$). This compound was synthesized through a modified literature procedure.[31] 2,3,5,6-Tetrabromo-1,4-benzoquinone (2.12 g, 5.00 mmol) was added as a solid to a solution of sodium acetate (0.600 g, 7.32 mmol) in a mixture of ethanol (50 mL), acetic acid (50 mL), and water (25 mL)

dx.doi.org/10.1021/ic5025586 | Inorg. Chem. 2015, 54, 359−369

to give a yellow mixture. Aniline (1.86 g, 20.0 mmol) was then added to this suspension, and the resulting dark brown mixture was heated at 110 °C for 5 h. The dark brown mixture was then filtered while hot, and the dark brown residue was washed with water (3 × 25 mL) and then dried at 50 °C under vacuum for 12 h to afford 2.15 g (96%) of product as a dark brown powder. ^{1}H NMR (DMSO-d_6, 500 MHz): δ 9.68 (s, 2H, NH), 7.34 (dd, 4H, aryl-H), 7.17−7.20 (m, 6H, aryl-H). FTIR (ATR, cm^{-1}): 3229 (m), 3051 (w), 1646 (w), 1600 (w), 1559 (s), 1493 (s), 1475 (s), 1443 (s), 1318 (s), 1308 (m), 1244 (m), 1141 (m), 1164 (m), 1150 (m), 1075 (m), 1016 (m), 1001 (w), 908 (m), 873 (m), 833 (m), 771 (s), 751 (s), 730 (s), 711 (s), 690 (s).

Sodium Tetrakis[3,5-bis(trifluoromethyl)phenyl]borate (Na(BAr^F)). This compound was prepared according to a modified literature procedure.[32] Mg turnings (10.0 g, 413 mmol), $NaBF_4$ (7.03 g, 64.0 mmol), and 1,2-dibromoethane (10.7 g, 57.0 mmol) were added to a round-bottom flask containing Et_2O (1.5 L). The mixture was heated to reflux in order to initiate the reaction, and once the mixture was at reflux, external heating was immediately ceased. The white mixture was stirred for 3 h, and then a solution of 3,5-bis(trifluoromethyl)bromobenzene (105 g, 360 mmol) in Et_2O (500 mL) was added dropwise over 3 h; the resulting mixture was heated at reflux for 1 h. The mixture was then allowed to cool to ambient temperature and stirred overnight. A solution of Na_2CO_3 (160 g) in water (2 L) was then added, and the resulting mixture was stirred for 1 h and then filtered to remove the remaining white insoluble material. After separation of the Et_2O layer, the remaining aqueous layer was washed with Et_2O (3 × 500 mL). All Et_2O layers were then combined, dried over Na_2SO_4, treated with decolorizing carbon (20.0 g), and dried under vacuum at 50 °C for 4 h. Under a dinitrogen atmosphere, the remaining oily residue was dissolved in benzene (200 mL) to give a pale yellow solution, and trace amounts of water were removed using a Dean−Stark apparatus. The resulting pale yellow solution was dried under vacuum for 12 h to give a pale yellow powder. This powder was washed with a 2:1 cold CH_2Cl_2/*n*-hexane mixture (4 × 10 mL) to remove the yellow color and then was dried at 110 °C under vacuum for 12 h to give 47.8 g (84%) of product as an off-white powder. ^{1}H NMR (DMSO-d_6, 500 MHz): δ 7.66 (s, 4H), 7.61 (br, 8H). FTIR (ATR, cm^{-1}): 1629 (w), 1612 (w), 1356 (s), 1280 (s), 1115 (br), 945 (w), 933 (w), 887 (m), 837 (m), 743 (w), 709 (m), 680 (m), 669 (m).

Thallium Tetrakis[3,5-bis(trifluoromethyl)phenyl]borate (Tl(BAr^F)). This compound was prepared according to a modified literature procedure.[33] A solution of Na(BAr^F) (2.57 g, 2.89 mmol) in EtOH (9 mL) was added to a solution of $TlNO_3$ (0.771 g, 2.89 mmol) in water (15 mL), and the resulting pale yellow solution was stirred at ambient temperature for 30 min. The solution was then concentrated under reduced pressure to a volume of 12 mL, resulting in the precipitation of an off-white solid. The precipitate was collected by filtration, washed with cold water (5 × 5 mL), and dried under vacuum at 110 °C for 12 h to give 2.31 g (75%) of product as a white powder. FTIR (ATR, cm^{-1}): 1629 (w), 1611 (w), 1356 (s), 1278 (s), 1118 (br), 943 (w), 933 (w), 886 (m), 837 (m), 743 (w), 709 (m), 680 (m), 669 (m).

Fe(BAr^F)$_2$·6MeCN. This compound was prepared according to a modified literature procedure.[34] A solution of $FeBr_2$ (63.3 mg, 0.293 mmol) in MeCN (6 mL) was added to a solution of Tl(BAr^F) (626 mg, 0.586 mmol) of MeCN (10 mL). The resulting yellow mixture was stirred at ambient temperature for 5 h and then filtered to remove a white insoluble material. The pale yellow filtrate was concentrated under vacuum to ∼1 mL and stored at −35 °C overnight to give white needle-shaped crystals. The crystals were immediately collected by filtration and washed with cold MeCN to give 145 mg (54%) of product. FTIR (ATR, cm^{-1}): 1611 (w), 1354 (s), 1276 (s), 1109 (br), 937 (w), 888 (m), 839 (m), 746 (w), 712 (m), 682 (m), 669 (m).

*[(TPyA)$_2$Fe$_2$(^{H}L)](BAr^F)$_2$·THF·n-Hexane (**1**).* TPyA (49.6 mg, 0.170 mmol) was dissolved in THF (2 mL), and this solution was added dropwise with stirring to a solution of Fe(BAr^F)$_2$·6MeCN (345 mg, 0.170 mmol) in THF (2 mL). The resulting red solution was stirred for 10 min at ambient temperature and then was treated with a suspension of ^{H}LH$_2$ (24.7 mg, 0.0850 mmol) in THF (4 mL) to give a dark brown mixture. To this mixture was added dropwise with stirring a solution of Na[N(SiMe$_3$)$_2$] (31.2 mg, 0.170 mmol) in THF (4 mL), resulting in a dark brown solution. After 12 h of stirring, the resulting dark green solution was filtered through diatomaceous earth. The filtrate was concentrated under reduced pressure to a volume of 2 mL. A portion of *n*-hexane (8 mL) was carefully layered onto the filtrate to give a dark green microcrystalline solid after 1 day, which was subsequently washed with cold EtOH (2 × 0.3 mL). The residue was dissolved in THF (2 mL) and recrystallized through layering with *n*-hexane (8 mL) to afford 172 mg (75%) of **1** as a dark green microcrystalline solid. FTIR (ATR, cm^{-1}): 2921 (w), 2859 (w), 1604 (w), 1575 (w), 1537 (m), 1485 (w), 1440 (w), 1352 (m), 1273 (s), 1243 (m), 1156 (s), 1116 (m), 1052 (m), 1019 (m), 862.71 (m), 828 (m), 780 (m), 743 (m), 715 (m), 699 (w), 681 (m), 668 (m). Anal. Calcd for $C_{118}H_{74}B_2F_{48}Fe_2N_{10}O_3$: C, 52.00; H, 2.74; N, 5.14%. Found: C, 51.75; H, 2.61; N, 4.76%. Dark green needle-shaped crystals of the related compound [(TPyA)$_2$Fe$_2$(^{H}L)](BAr^F)$_2$·4Et$_2$O] (**1′**), suitable for single-crystal X-ray diffraction, were obtained through diffusion of Et_2O vapor into a THF solution.

*[(TPyA)$_2$Fe$_2$(^{Br}L)](BAr^F)$_2$·THF·n-Hexane (**2**).* This compound was synthesized analogously to **1** using TPyA (49.6 mg, 0.170 mmol), Fe(BAr^F)$_2$·6MeCN (345 mg, 0.170 mmol), ^{Br}LH$_2$ (38.1 mg, 0.0850 mmol), and Na[N(SiMe$_3$)$_2$] (31.2 mg, 0.170 mmol). Layering of the filtrate with *n*-hexane (8 mL) yielded a mixture of dark green and white microcrystalline solid, which was washed with cold EtOH (2 × 0.3 mL) to remove the white solid. The remaining dark green solid was dissolved in THF (2 mL) and recrystallized through layering with *n*-hexane (8 mL) to afford 194 mg (80%) of **2** as dark green needle-shaped crystals suitable for single-crystal X-ray diffraction. FTIR (ATR, cm^{-1}): 2923 (w), 2858 (w), 1605 (w), 1511 (m), 1484 (m), 1440 (w), 1352 (s), 1272 (s), 1155 (s) 1113 (s), 1053 (m), 1020 (w), 886 (m), 874.71 (m), 837 (m), 762 (m), 743 (w), 715 (w), 695 (w), 681 (m), 668 (m). Anal. Calcd for $C_{126}H_{86}B_2Br_2F_{48}Fe_2N_{10}O_4$: C, 50.29; H, 2.88; N, 4.65%. Found: C, 50.51; H, 2.46; N, 4.67%.

*[(TPyA)$_2$Fe$_2$(^{Cl}L)](BAr^F)$_2$·THF·n-Hexane (**3**).* This compound was synthesized analogously to **1** using TPyA (49.6 mg, 0.170 mmol), Fe(BAr^F)$_2$·6MeCN (345 mg, 0.170 mmol), ^{Cl}LH$_2$ (30.5 mg, 0.0850 mmol), and Na[N(SiMe$_3$)$_2$] (31.2 mg, 0.170 mmol). Layering of the filtrate with *n*-hexane (8 mL) yielded a mixture of dark green and white microcrystalline solid, which was washed with cold EtOH (2 × 0.3 mL) to remove the white solid. The remaining dark green solid was redissolved in THF (2 mL) and recrystallized through layering with *n*-hexane (8 mL) to afford 166 mg (70%) of **3** as dark green needle-shaped crystals suitable for single-crystal X-ray diffraction. FTIR (ATR, cm^{-1}): 2922 (w), 2858 (w), 1605 (w), 1512 (m), 1484 (w), 1440 (w), 1352 (m), 1272 (s), 1156 (s) 1114 (m), 1053 (m), 1020 (m), 996 (m), 886 (m), 837 (m), 784 (m), 761 (m), 744 (m), 714 (w), 697 (m), 681 (m). Anal. Calcd for $C_{122}H_{78}B_2Cl_2F_{48}Fe_2N_{10}O_3$: C, 51.45; H, 2.76; N, 4.92%. Found: C, 51.55; H, 2.84; N, 4.58%.

*[(TPyA)$_2$Fe$_2$(^{F}L)](BAr^F)$_2$·THF·n-Hexane (**4**).* This compound was synthesized analogously to **1** using TPyA (49.6 mg, 0.170 mmol), Fe(BAr^F)$_2$·6MeCN (345 mg, 0.170 mmol), ^{F}LH$_2$ (27.7 mg, 0.0850 mmol), and Na[N(SiMe$_3$)$_2$] (31.2 mg, 0.170 mmol). Layering of the filtrate with *n*-hexane (8 mL) yielded a mixture of dark green and white microcrystalline solid, which was washed with cold EtOH (2 × 0.3 mL) to remove the white solid. The remaining dark green solid was dissolved in THF (2 mL) and recrystallized through layering with *n*-hexane (8 mL) to afford 179 mg (77%) of **4** as a dark green microcrystalline solid. FTIR (ATR, cm^{-1}): 2921 (w), 2859 (w), 1606 (w), 1542 (m), 1484 (w), 1441 (w), 1352 (m), 1330 (m), 1272 (s), 1224 (s), 1156 (s), 1115 (s), 1052 (m), 1008 (m), 904 (w), 886 (m), 837 (m), 761 (m), 743 (w), 716 (m), 700 (m), 681 (m), 668 (m). Anal. Calcd for $C_{122}H_{78}B_2F_{50}Fe_2N_{10}O_3$: C, 52.05; H, 2.82; N, 4.79%. Found: C, 51.92; H, 2.57; N, 5.11%. Dark green needle-shaped crystals of the related compound [(TPyA)$_2$Fe$_2$(^{F}L)](BAr^F)$_2$·4Et$_2$O (**4′**), suitable for single-crystal X-ray diffraction, were obtained through diffusion of Et_2O vapor into a THF solution.

X-ray Structure Determination. Single crystals of **1′**, **2**, **3**, and **4′** were coated with deoxygenated Paratone-N oil, mounted on a

dx.doi.org/10.1021/ic5025586 | Inorg. Chem. 2015, 54, 359−369

Table 1. Crystallographic Data for 1′, 2, 3, and 4′

	1′		2		3		4′	
formula	$C_{134}H_{112}B_2F_{48}Fe_2N_{10}O_6$		$C_{128}H_{92}B_2Br_2F_{48}Fe_2N_{10}O_3$		$C_{124}H_{84}B_2Cl_2F_{48}Fe_2N_{10}O_3$		$C_{134}H_{110}B_2F_{50}Fe_2N_{10}O_6$	
fw (g/mol)	3003.65		3023.25		2934.33		3039.63	
T (K)	100	225	100	225	100	225	100	225
space group	$P\bar{1}$	$P\bar{1}$	$P\bar{1}$	$P\bar{1}$	$P\bar{1}$	$P\bar{1}$	$P\bar{1}$	$P\bar{1}$
Z	1	1	1	1	1	1	1	1
a (Å)	12.1891(9)	12.3247(6)	12.3771(7)	12.4619(5)	12.2621(8)	12.3707(5)	12.1907(7)	12.2877(5)
b (Å)	16.250(1)	16.9752(6)	16.844(1)	17.1585(8)	16.824(1)	17.2025(7)	16.6435(9)	16.8312(7)
c (Å)	17.898 (2)	17.7140(9)	17.592(1)	17.9518(8)	17.610(1)	17.9700(8)	17.3578(9)	17.7318(8)
α (deg)	88.042(5)	86.386(2)	85.473(2)	84.820(2)	85.809(3)	84.892(2)	87.671(2)	87.114(2)
β (deg)	74.917(3)	75.656(2)	76.051(2)	76.042(2)	76.479(3)	76.314(1)	77.622(2)	76.717(1)
γ (deg)	79.386(3)	76.244(1)	78.445(2)	77.842(2)	77.825(3)	77.330(2)	77.463(2)	77.569(2)
V (Å^3)	3364.1(5)	3487.5(3)	3485.5(3)	3638.5(3)	3451.7(4)	3622.3(3)	3357.9(3)	3485.4(3)
d_{calc} (g/cm^3)	1.483	1.430	1.395	1.380	1.412	1.345	1.503	1.448
R_1 ($I > 2\sigma(I)$)[a]	8.79	7.41	5.65	6.63	9.95	7.14	8.57	6.49
wR_2 (all)[b]	26.62	22.82	17.35	20.79	28.50	22.65	24.27	20.56
GoF	1.078	1.101	1.083	1.079	1.029	1.140	1.084	1.105

[a] $R_1 = \sum||F_0| - |F_C||/\sum|F_0|$. [b] $wR_2 = [\sum w(F_0^2 - F_C^2)^2/\sum w(F_0^2)^2]^{1/2}$.

Scheme 1. Synthesis of Compounds $[(TPyA)_2Fe_2(^XL)](BAr^F)_2$ (X = H, Br, Cl, and F)

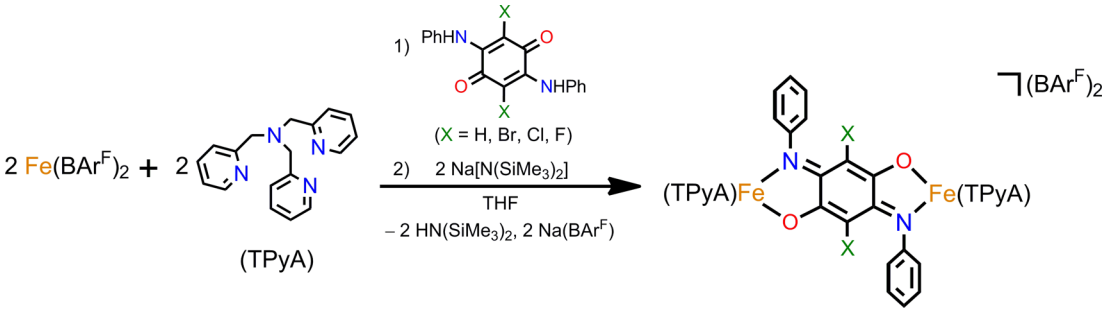

MicroMounts rod, and frozen under a stream of N_2 during data collection. Crystallographic data were collected at 225 K using a Bruker Kappa Apex II diffractometer equipped with an APEX-II detector, a Cu Kα microfocus source, and either Quazar Optics (for **1**′ and **2**) or MX Optics (for **3** and **4**′). Crystallographic data were also collected at 100 K using a Bruker Kappa Apex II diffractometer equipped with an APEX-II detector, a Cu Kα microfocus source, and MX Optics for **1**′, **2**, and **4**′, and a Bruker Kappa Apex II diffractometer equipped with an APEX-II detector and a Mo Kα sealed-tube source for **3**. Raw data were integrated and corrected for Lorentz and polarization effects with SAINT v8.27B.[35] Absorption corrections were applied using SADABS.[36] Space group assignments were determined by examination of systematic absences, E-statistics, and successive refinement of the structure. Structures were solved using direct methods in SHELXS and further refined with SHELXL-2013[36] operated with the OLEX2 interface.[37] All hydrogen atoms were placed at calculated positions using suitable riding models and refined using isotropic displacement parameters derived from their parent atoms. Thermal parameters were refined anisotropically for all non-hydrogen atoms. Crystallographic data for **1**′, **2**, **3**, and **4**′ at 100 and 225 K are given in Table 1. Significant disorder of the $-CF_3$ groups on the $[BAr^F]^-$ anions was modeled with partial occupancies; however, some disorder that did not improve the final refinement of the solution was placed at one position with full occupancy. The interstitial THF molecules in **2** (100 and 225 K) and **3** (100 K) and the Et_2O molecules in **1**′ (100 K) and **4**′ (100 K) required distance and displacement parameter restraints because of disorder, and the associated hydrogen atoms were not placed but were included in the final chemical formulas. All solvent molecules in **1**′, **3**, and **4**′ at 225 K and the *n*-hexane molecules in **2** (100 and 225 K) and **3** (100 K) were severely disordered and could not be modeled properly. These species were therefore treated as a diffuse contribution to the overall scattering without specific atom positions using the solvent masking procedure implemented in OLEX2. These molecules were included in the final molecular formula.

Magnetic Measurements. All samples were prepared and manipulated with the rigorous exclusion of dioxygen, either under a dinitrogen atmosphere or under vacuum. Magnetic measurements of **1**–**4** were performed on polycrystalline samples retained in their original THF/*n*-hexane mother liquor loaded into quartz tubes. The quartz tube was fixed to a sealable hose-adapter, degassed through three successive freeze–pump–thaw cycles, evacuated on a Schlenk line while frozen in liquid N_2, and then flame-sealed. All data were collected using a Quantum Design MPMS-XL SQUID magnetometer from 1.8 to 300 K at applied dc fields ranging from 0 to +7 T. Variable-temperature data were collected at a scan rate of ∼1 K/min at 1 T and of ∼2 K/min at 0.1 T. dc susceptibility data were corrected for diamagnetic contributions from the sample holder and for the core diamagnetism of each sample (estimated using Pascal's constants[38]). M(H) curves constructed from data collected from 0 to 4 T at 100 K confirmed the absence of ferromagnetic impurities in all samples.

Mössbauer Measurements. Zero-field iron-57 Mössbauer spectra were obtained between 80 and 250 K with a constant acceleration spectrometer and a cobalt-57 rhodium source. Prior to measurements, the spectrometer was calibrated at 295 K with α-iron foil. Samples were prepared in a dinitrogen-filled glovebox with crystals of **1**–**4** that were quickly filtered and inserted into the cryostat prior to the measurement. Each sample contained approximately 80 mg/cm^2 of compound. All spectra were analyzed using the WMOSS Mössbauer Spectral Analysis Software (www.wmoss.org). Fits to a minor doublet in the spectra of **1**–**4** at 250 K gave an isomer shift of δ = 0.23(1)–0.25(1) mm/s and a quadrupole splitting of ΔE_Q = 0.30(2)–0.39(2) mm/s, consistent with a small amount of high-spin Fe^{III}-containing impurity in the sample. To fit the spectra of **4** at 100 and 80 K, the

dx.doi.org/10.1021/ic5025586 | Inorg. Chem. 2015, 54, 359–369

upper limit of ΔE_Q for the quadrupole doublet assigned to the high-spin Fe^{II} site in the $[Fe_{HS}\text{-}Fe_{LS}]$ species was fixed to 2.93 and 3.02 mm/s, respectively, due to the otherwise unstable fit.

Other Physical Measurements. Elemental analyses of all compounds were performed by the Midwest Microlab (Indianapolis, IN). Infrared spectra were recorded on a Bruker Alpha Fourier transform infrared (FTIR) spectrometer equipped with an attenuated total reflectance accessory. ^1H NMR spectra were collected at 500 MHz on a Varian Inova 500 system at 298 K.

RESULTS AND DISCUSSION

Syntheses and Structures. The bridging ligands $^{X}LH_2$ were synthesized by reaction of aniline with 1,4-benzoquinone (X = H[29]) or the corresponding 2,3,5,6-tetrahalo-1,4-benzoquinone (X = F,[30] Cl,[31] Br[31]) following modified literature procedures. The deprotonated benzoquinone derivative ($^{X}L^{2-}$) was generated in solution by reaction of $^{X}LH_2$ with 2 equiv of $Na[N(SiMe_3)_2]$ in THF (see Scheme 1). Metalation of this species with Fe^{II} was then effected by treatment with a THF solution containing 2 equiv each of tris(2-pyridylmethyl)-amine (TPyA) and $Fe(BAr^F)_2$ ($[BAr^F]^-$ = tetrakis[3,5-bis-(trifluoromethyl)phenyl]borate anion) to give a dark green solution. Subsequent careful layering of this solution with *n*-hexane resulted in the cocrystallization of dark green needle-shaped crystals and colorless crystals of $NaBAr^F$. The $NaBAr^F$ side product was then removed by successive washing with minimal amounts of EtOH that had been cooled to −78 °C, giving rise to pure dark green crystalline material. Finally, this material was recrystallized via *n*-hexane layering on THF solutions to yield dark green needle-shaped crystals of $[(TPyA)_2Fe_2(^{X}L)](BAr^F)_2\cdot THF\cdot n\text{-hexane}$ (X = H (**1**), Br (**2**), Cl (**3**), and F (**4**)). Note that metal complexes featuring derivatives of 2,5-dianilino-1,4-benzoquinone[39−42] as bridging ligands are far less common than those of the isoelectronic 2,5-dihydroxy-1,4-benzoquinone derivatives.[20−26] Indeed, to our knowledge, **1**−**4** represent the first examples of Fe complexes of a 2,5-dianilino-1,4-benzoquinone derivative.

Single crystals suitable for X-ray diffraction analysis were obtained for **2** and **3** through the layering method described above. In contrast, this method gave crystals of **1** and **4** that were not of sufficient quality to enable collection of a complete data set. Nevertheless, unit cell determinations confirmed that these compounds are indeed isostructural to **2** and **3** (Table S1, Supporting Information). Alternatively, diffusion of diethyl ether vapor into THF solutions containing **1** and **4** gave dark green needle-shaped crystals of $[(TPyA)_2Fe_2(^{X}L)](BAr^F)_2\cdot 4Et_2O$ (X = H (**1′**) and F (**4′**)) suitable for single-crystal X-ray diffraction analysis. Note that the relatively high solubility of **2** and **3** in Et_2O prohibited crystallization of the analogous compounds **2′** and **3′**.

Single-crystal X-ray diffraction analysis for **1′**, **2**, **3**, and **4′** was carried out at both 225 and 100 K to probe for structural changes associated with spin crossover. At both temperatures, all compounds crystallize in the triclinic space group $P\bar{1}$ and are isostructural to one another (Table 1). The general structure of $[(TPyA)_2Fe_2(^{X}L)]^{2+}$ comprises a dinuclear Fe^{II}_2 complex in which two crystallographically equivalent $[(TPyA)Fe]^{2+}$ units are connected by a dianionic $^{X}L^{2-}$ bridging ligand with a crystallographic site of inversion located at the center of the bridging ligand (Figure 1 and Figures S1−S3 of the Supporting Information). Each Fe^{II} center resides in a distorted octahedral coordination environment made up of four nitrogen donor atoms from the TPyA capping ligand and cis-disposed nitrogen and oxygen donor atoms from the bridging ligand.

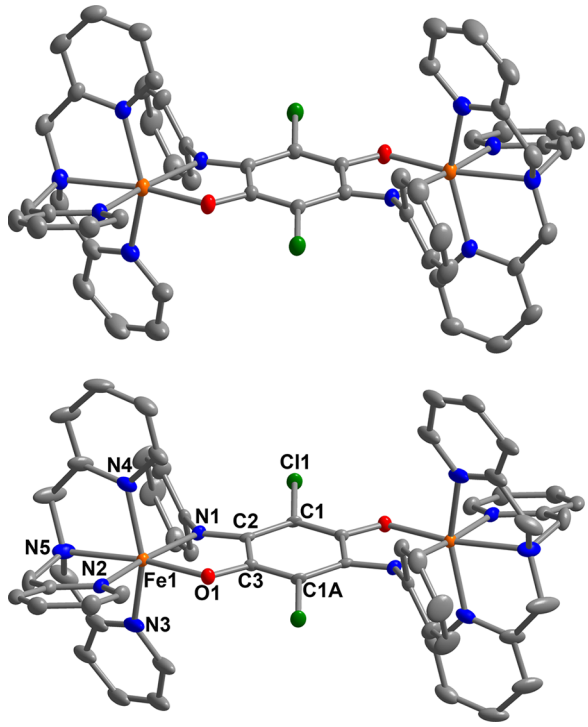

Figure 1. Crystal structure of $[(TPyA)_2Fe_2(^{Cl}L)]^{2+}$ at 100 (bottom) and 225 K (top), as observed in **3**, with ellipsoids shown at the 40 and 20% probability level, respectively. Colored ellipsoids represent Fe (orange), Cl (green), O (red), N (blue), and C (gray) atoms. H atoms are omitted for clarity.

At 225 K, the average $Fe\text{−}N_{TPyA}$, $Fe\text{−}N_L$, and Fe−O distances across the series fall in the ranges of 2.185(3)−2.189(3), 2.148(3)−2.171(2), and 1.997(2)−2.002(2) Å, respectively, which is consistent with the presence of two high-spin $S = 2$ Fe^{II} centers (Table 2). Within the bridging ligand, the O1−C3 and N1−C2 bond distances of 1.288(4)−1.359(4) and 1.297(4)−1.306(4) Å, respectively, are longer than a C=O double bond and shorter than a C−N single bond. Moreover, the C1−C2 bond lengths of 1.413(5)−1.425(4) Å are longer than the C3−C1A bond lengths of 1.361(4)−1.368(5) Å. Finally, the C2−C3 bond distances are in the range of 1.505(5)−1.516(4) Å across the series, which is typical for a C−C single bond. These collective distances suggest that $^{X}L^{2-}$ is comprised of localized 6-π-electron fragments connected by two C−C single bonds. Furthermore, these distances are consistent with each Fe^{II} center being ligated by an oxygen atom of a deprotonated hydroxy group and a nitrogen atom of a neutral imine group, such that $^{X}L^{2-}$ is best described as a bis(phenolate)diimine derivative. Likely, this composition results from better stabilization of negative charges afforded by the more electronegative oxygen atoms. Indeed, a similar observation was previously reported for Co^{II}_2 and Ru^{II}_2 complexes bridged by 2,5-diarylamino-1,4-benzoquinone derivatives.[39−42]

At 100 K, crystals of **1′**, **2**, **3**, and **4′** maintain their space group of $P\bar{1}$, albeit with slightly decreased unit cell dimensions relative to the 225 K data (Table 1). Close inspection of the diffraction images for the crystal of **1′** revealed a splitting of Bragg peaks along nonspecific crystallographic directions, and extraction of unit cell parameters for these new peaks was not possible (Figure S4, Supporting Information). The splitting at low temperature did not correspond to physical cracking of the

dx.doi.org/10.1021/ic5025586 | Inorg. Chem. 2015, 54, 359−369

Table 2. Selected Interatomic Distances (Å) and Angles (deg) for 1′, 2, 3, and 4′[a]

	1′	2		3		4′	
T (K)	225	100	225	100	225	100	225
Fe−N2	2.141(3)	2.168(3)	2.169(3)	2.077(3)	2.167(3)	2.152(4)	2.165(3)
Fe−N3	2.162(3)	2.040(3)	2.145(4)	2.053(4)	2.148(3)	2.149(4)	2.144(3)
Fe−N4	2.161(3)	2.056(4)	2.141(3)	2.060(3)	2.150(4)	2.134(3)	2.160(3)
Fe−N5	2.290(3)	2.168(3)	2.283(3)	2.179(4)	2.276(3)	2.261(4)	2.288(3)
Fe−$N_{TPyA,avg}$	2.188(3)	2.106(3)	2.185(3)	2.093(3)	2.185(3)	2.174(4)	2.189(3)
Fe−N1	2.148(3)	2.108(3)	2.158(3)	2.092(3)	2.163(3)	2.149(3)	2.171(2)
Fe−O1	1.999(2)	1.964(2)	1.997(2)	1.972(2)	1.997(2)	1.997(3)	2.002(2)
Fe−Fe_{intra}[b]	7.9994(8)	7.9680(8)	8.0561(8)	7.9688(8)	8.0538(8)	8.0080(9)	8.0360(7)
Fe−Fe_{inter}[c]	12.325(1)	12.2595(9)	12.3491(8)	12.251(1)	12.3331(8)	12.191(1)	12.2877(9)
C1−C2	1.421(5)	1.419(4)	1.423(5)	1.413(5)	1.425(4)	1.417(6)	1.415(4)
C2−C3	1.505(5)	1.502(4)	1.510(4)	1.504(4)	1.516(4)	1.506(6)	1.508(4)
C3−C1A	1.361(4)	1.374(4)	1.368(5)	1.365(5)	1.367(4)	1.362(6)	1.362(4)
N1−C2	1.306(4)	1.313(4)	1.302(4)	1.324(4)	1.297(4)	1.300(5)	1.303(4)
O1−C3	1.359(4)	1.292(4)	1.288(4)	1.290(4)	1.292(4)	1.294(5)	1.292(3)
Σ[d]	122.9(3)	98.7(3)	123.5(3)	102.4(3)	123.8(3)	116.9(3)	123.8(3)

[a]See Figure 1 and Figures S5−S7 in the Supporting Information for the atomic numbering scheme. [b]Intramolecular Fe···Fe distance. [c]Shortest intermolecular Fe···Fe distance. [d]Octahedral distortion parameter (Σ) = sum of the absolute deviations from 90° of the 12 cis angles.

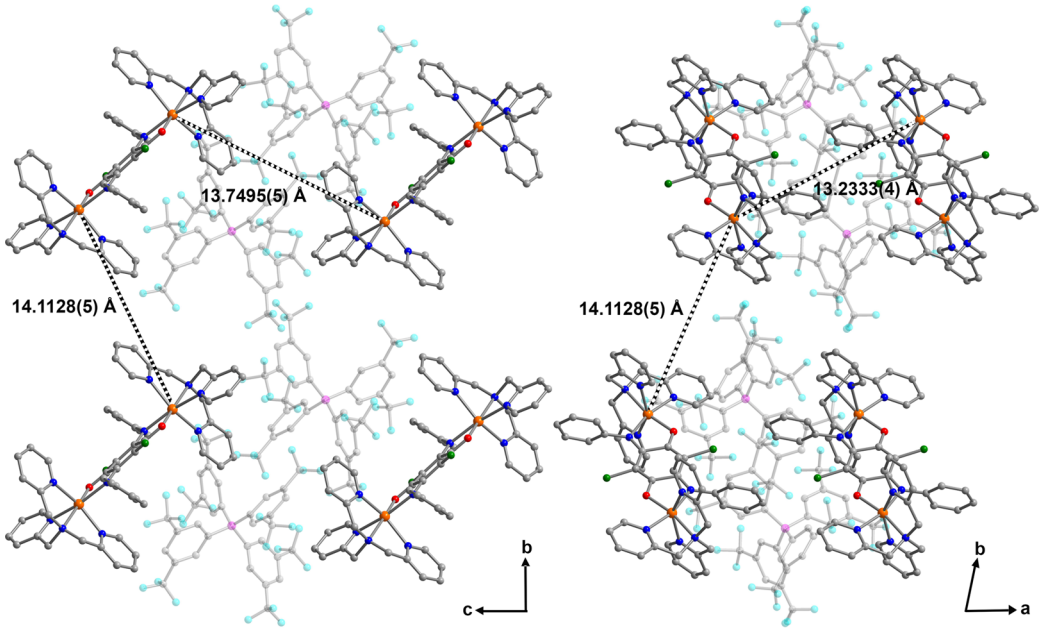

Figure 2. Portion of the crystal structure of **3** at 225 K, as viewed normal to the *cb* (left) and *ab* (right) planes, highlighting the large intermolecular separation of dicationic Fe_2 complexes afforded by bulky $[BAr^F]^-$ anions. Colored spheres represent Fe (orange), Cl (green), F (turquoise), O (red), N (blue), C (gray), and B (magenta) atoms. For clarity, H atoms and solvent molecules are omitted, and $[BAr^F]^-$ anions are shown as translucent. Black dotted lines denote the shortest intermolecular Fe···Fe distances.

crystal; it possibly stemmed from long-range structural disorder of the low-spin state.[43] A structure solution obtained from the averaged peak assignment confirmed the connectivity of a cationic complex; however, determination of interatomic distances and angles was not possible. As such, the structure of **1**′ at 100 K will not be considered in future discussion.

Comparison of the bond distances at 100 and 225 K reveals several key differences. First, at 100 K, the average Fe−N_{TPyA} distances were found to decrease substantially to 2.106(3), 2.093(3), and 2.174(4) Å for **2**−**4**′, respectively. In addition, the Fe−N_L and Fe−O bonds also exhibited considerably shorter distances of 2.108(3) and 1.964(2), 2.092(3) and 1.972(2), and 2.149(3) and 1.997(3) Å for **2**−**4**′, respectively (Table 2). The decreased bond distances in **2** and **3**, while too short to correspond to high-spin Fe^{II}, are nevertheless longer than those expected for two low-spin Fe^{II} centers per dinuclear complex.[39] This observation suggests the presence of a mixture of high- and low-spin Fe^{II} centers at 100 K, possibly resulting from incomplete spin crossover. Along these lines, the average Fe−N_{TPyA}, Fe−N_L, and Fe−O bond distances in **2** and **3** are quite similar, both intermediate between those expected for low-spin and high-spin states, suggesting the presence of a near equimolar population of low-spin and high-spin Fe^{II} centers. In contrast, the distances observed in **4**′ fall much closer to the high temperature values, suggesting a majority of high-spin Fe^{II} centers in **4**′ at 100 K. This comparative observation is not surprising given the electron-withdrawing nature of the more electronegative fluorine substituent, which apparently serves to

dx.doi.org/10.1021/ic5025586 | Inorg. Chem. 2015, 54, 359−369

stabilize the high-spin state. Although the bond distances in **2**–**4**′ suggest a mixture of low-spin and high-spin Fe^{II} centers in the crystal at 100 K, the presence of only one $[(TPyA)Fe]^{2+}$ moiety in the asymmetric unit complicates further differentiation between the presence of mixed-spin-state dinuclear $[Fe_{HS}\text{-}Fe_{LS}]$ complexes and a mixture of single-spin-state $[Fe_{HS}\text{-}Fe_{HS}]$ and $[Fe_{LS}\text{-}Fe_{LS}]$ complexes (further discussion below).

Compounds **1**′, **2**, **3**, and **4**′ feature intramolecular Fe···Fe distances in the range of 7.999(1)–8.056(1) Å at 225 K and 7.968(1)–8.008(1) Å at 100 K. In the overall structures, the 2+ charge of each Fe_2 is compensated for by two noncoordinating $[BAr^F]^-$ counteranions (Figure 2 and Figures S5–S7 in the Supporting Information). These bulky anions interact with the Fe_2 complexes through a number of hydrogen-bonding interactions, evident from contacts of $^XL^{2-}$ phenyl- and TPyA-based carbon atoms with $-CF_3$ groups of $[BAr^F]^-$, with the shortest intermolecular C···F distances in the range of 2.91(1)–3.14(1) Å across the series at 225 K. The presence of such bulky anions engenders a large separation between Fe_2 complexes in the solid state, with the shortest intermolecular Fe···Fe distances across the series of 12.2877(5)–12.349(1) Å at 225 K and 12.191(1)–12.259(3) Å at 100 K. Importantly, this large intermolecular separation should enable the evaluation of electronic effects on spin crossover with minimal complications from intermolecular cooperative interactions that are likely to be similar across the series.

Compounds **1**′, **2**, **3**, and **4**′ contain rare examples of spin crossover Fe^{II} complexes that feature an $[N_5O]$ local coordination environment.[5b,45] At each Fe center, the presence of an Fe–O distance that is significantly shorter than the Fe–N distances leads to a severely distorted coordination environment. This distortion from an ideal octahedron can be quantified through the parameter Σ, which is defined as the sum of the absolute deviations of each of the 12 cis-disposed L–Fe–L angles from 90°.[46] Analysis of the Fe centers in **1**′, **2**, **3**, and **4**′ at 225 K gives values of Σ = 122.9(3), 123.5(3), 123.8(3), and 123.8(3), respectively. As discussed above, the pathway of spin crossover in dinuclear complexes has been proposed to be highly dependent on the degree of distortion at the Fe^{II} center.[17,19] Indeed, a recent report summarized the correlation of spin crossover and values of Σ for a number of known dinuclear Fe^{II} complexes.[17] This study demonstrated a general trend that complexes with Σ < 40 invariably undergo complete spin crossover from high-spin to low-spin states without the presence of any intermediate state. In contrast, those complexes with Σ > 120 were found to exhibit incomplete spin crossover involving an intermediate state of mixed-spin $[Fe_{HS}\text{-}Fe_{LS}]$ composition. Accordingly, the high values of Σ in **1**′, **2**, **3**, and **4**′ are consistent with the hypothesis that these complexes undergo incomplete spin crossover involving an intermediate state.

Magnetic Properties. To probe and compare the presence of spin crossover in compounds **1**–**4**, variable-temperature dc magnetic susceptibility data were collected in the temperature range of 1.8–300 K on crystalline samples retained in their original THF/*n*-hexane mother liquor to prevent partial desolvation. The resulting plots of $\chi_M T$ vs T are shown in Figure 3 (see also Figure S8 in the Supporting Information). At 300 K, compounds **1**–**4** exhibit values ranging from $\chi_M T$ = 6.74 (for **4**) to 6.83 (for **1**) $cm^3\ mol^{-1}\ K$, corresponding to two non-interacting high-spin S = 2 Fe^{II} centers with g = 2.12–2.13. As the temperature is decreased, the data initially remain relatively constant before undergoing a gradual decline to minima values

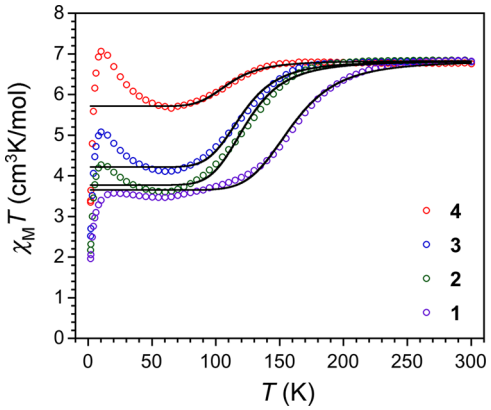

Figure 3. Variable-temperature dc magnetic susceptibility data for solid samples of **1**–**4** collected under an applied field of 1 T. Circles represent experimental data, whereas black lines correspond to fits based on an ideal solution model as described in the text.

of $\chi_M T$ near 50 K. Although the S-shaped $\chi_M T$ curve is a signature of spin crossover, the non-zero minimum values of $\chi_M T$ at low temperature indicate that a considerable number of Fe^{II} centers remain trapped in the high-spin state. The overall shape of the data and the minimum values of $\chi_M T$ suggest an incomplete spin crossover, and this conversion may be kinetically slower or highly impeded with increasing electronegativity of X on $^XL^{2-}$. Indeed, similar partial trapping of high-spin Fe centers was previously observed for a number of mononuclear[47] and some dinuclear complexes.[48] The temperature at which a discrepancy from the high-temperature plateau appears decreases across the series from **1** to **4** and therefore demonstrates larger stabilization of the high-spin state by a more electronegative substituent on the bridging ligand. Finally, note that these observations are consistent with the bond distances of Fe ascertained from single-crystal X-ray diffraction analysis.

To quantify the spin crossover phenomena in **1**–**4**, the data were fit to the ideal solution model[49,50] to give crossover temperatures ($T_{1/2}$) of 160(1), 124(1), 121(1), and 110(1) K and percentages of high-spin states of Fe^{II} centers at low temperature of 54(1), 56(1), 62(1), and 84(1) for **1**, **2**, **3**, and **4**, respectively (see Table 3). Importantly, the observed trend

Table 3. Summary of Parameters Obtained from Fits to Magnetic Data[a]

	ΔH (kJ/mol)	ΔS (J/mol·K)	$T_{1/2}$ (K)	$Fe_{HS,trapped}$ (%)
1	11.4(3)	71(2)	160(1)	54(1)
2	8.5(3)	69(3)	124(1)	56(1)
3	8.3(3)	69(2)	121(1)	62(1)
4	7.5(2)	68(2)	110(1)	84(1)

[a]Fits obtained using an ideal solution model as described in the text.

scales with electronegativity of X on $^XL^{2-}$, with increasingly electronegative substituents providing better stabilization for high-spin Fe^{II} centers. Indeed, the presence of these relatively remote substituents remarkably decreases the crossover temperature by 50 K, or more than 31%, in moving from X = H to X = F.

In addition to $T_{1/2}$, fits to the data also provide estimates of thermodynamic parameters for **1**–**4** of ΔH = 11.4(3), 8.5(3), 8.3(3), and 7.5(2) kJ/mol and ΔS = 71(2), 68(3), 69(2), and 68(2) J/mol·K, respectively; these values are similar in

dx.doi.org/10.1021/ic5025586 | *Inorg. Chem.* 2015, 54, 359–369

magnitude to others previously reported for spin crossover Fe^{II} complexes (Table 3).[51] Across the series, ΔH decreases by 34%, whereas ΔS decreases by only 4%. This comparison suggests that the observed differences in $T_{1/2}$ can be attributed primarily to changes in enthalpy rather than entropy. This trend is indicative of a direct correlation between $T_{1/2}$ of the spin crossover and differences in the ligand field at Fe^{II} stemming from substituent variation in $^{X}L^{2-}$. Overall, the difference in ΔH across the series is 3.9 kJ/mol, or 330 cm^{-1}, which can be considered as the relative decrease in the energy gap between $S = 0$ and $S = 2$ spin states in moving from **1** to **4**.

The correlation between thermodynamics of spin crossover and electronic character of $^{X}L^{2-}$ can be further examined by plotting $T_{1/2}$ and ΔH as a function of the Pauling electronegativity parameter (χ_P) of each X substituent (Figure 4).[52]

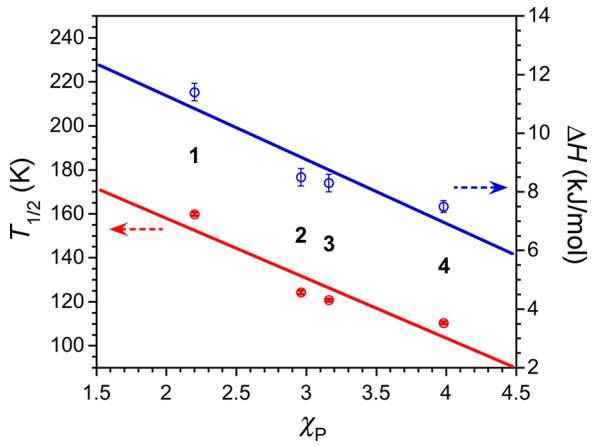

Figure 4. Plot of $T_{1/2}$ (red circles) and ΔH (blue circles) as a function of Pauling electronegativity (χ_P) for **1**–**4**. Solid lines correspond to linear fits to the data with equations of the best linear fit providing R^2 = 0.93 and 0.92, respectively.

Plots of both $T_{1/2}$ vs χ_P and ΔH vs χ_P follow nearly linear trends, with linear fits giving coefficients of determination of R^2 = 0.93 and 0.92, respectively. This observation suggests that the ligand field at Fe in this series of complexes is determined primarily by inductive effects, propagated through bonds and/or through space, of the different substituents. Note that this trend is inversely related to that previously observed for six-coordinate spin crossover Fe^{II} complexes featuring substituted pyridyl ligands, which behave primarily as π acceptors.[10−12]

Finally, as temperature is further decreased, the $\chi_M T$ data eventually undergo an increase and then a precipitous decrease, with maximum values of $\chi_M T$ = 3.53, 4.29, 5.07, and 7.05 cm^3 K mol^{-1} at 10 K for **1**–**4**, respectively. This increase in the $\chi_M T$ data with decreasing temperature is almost certainly the result of intramolecular ferromagnetic exchange coupling between two high-spin Fe^{II} centers. Moreover, the maximum value of $\chi_M T$ at 10 K increases with decreasing $T_{1/2}$ across the series from **1** to **4**. This trend perhaps lends insight into the nature of the incomplete spin crossover, in particular whether the intermediate state primarily comprises a mixed-spin [Fe_{HS}-Fe_{LS}] composition or a mixture of [Fe_{HS}-Fe_{HS}] and [Fe_{LS}-Fe_{LS}] species. Indeed, the data for **1** show almost no increase below 50 K. This observation strongly suggests that **1** features nearly exclusively [Fe_{HS}-Fe_{LS}] complexes below 50 K, as the alternative would most likely lead to a significant upturn in the data. Moreover, if compounds **2**–**4** behave similarly, then they should be comprised solely of [Fe_{HS}-Fe_{LS}] and [Fe_{HS}-Fe_{HS}] complexes.

To test this hypothesis, the number of high-spin Fe^{II} centers corresponding to [Fe_{HS}-Fe_{HS}] complexes, assuming the absence of any [Fe_{LS}-Fe_{LS}] complexes, can be calculated from the total number of high-spin centers at low temperature as extracted from fits to the magnetic data (Table 3). This treatment reveals that 7, 11, 23, and 67% of all high-spin Fe centers correspond to molecules of [Fe_{HS}-Fe_{HS}] composition in **1**–**4**, respectively. Assuming an $S = 4$ ground state with $g = 2.00$ for each [Fe_{HS}-

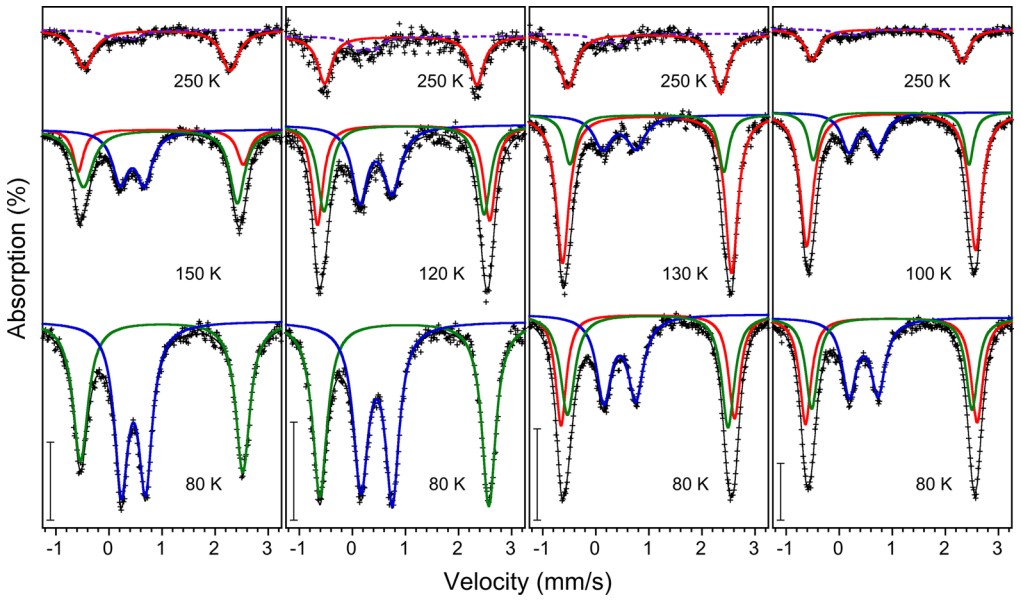

Figure 5. Zero-field Mössbauer spectra for crystalline samples of **1**–**4** (left to right, respectively) at selected temperatures. Black crosses represent experimental data, and gray solid lines correspond to overall fits. Colored solid lines correspond to individual components of the overall fits assigned to [Fe_{HS}-Fe_{HS}] (red), the high-spin center in [Fe_{HS}-Fe_{LS}] (green), and the low-spin center in [Fe_{HS}-Fe_{LS}] (blue). The dashed purple line corresponds to a fit assigned to a small amount of Fe^{III}-containing impurity. Each vertical scale bar represents an absorption of 1%.

dx.doi.org/10.1021/ic5025586 | Inorg. Chem. 2015, 54, 359−369

Table 4. Summary of Parameters Obtained from Fits to Mössbauer Spectra

		high-spin site in [Fe_{HS}-Fe_{HS}]			high-spin site in [Fe_{HS}-Fe_{LS}]			low-spin site in [Fe_{HS}-Fe_{LS}]		
	T (K)	δ (mm/s)	ΔE_Q (mm/s)	area (%)	δ (mm/s)	ΔE_Q (mm/s)	area (%)	δ (mm/s)	ΔE_Q (mm/s)	area (%)
1	80				0.99(1)	3.06(1)	49(2)	0.46(1)	0.45(1)	51(1)
	150	0.98(1)	3.10(7)	21(20)	0.97(1)	2.89(13)	44(27)	0.44(1)	0.45(1)	34(1)
	250	0.91(1)	2.74(2)	84(4)						
2	80				0.98(1)	3.18(1)	51(1)	0.46(1)	0.59(1)	49(1)
	120	0.96(1)	3.24(5)	34(20)	0.98(1)	3.01(10)	33(19)	0.44(1)	0.61(2)	33(2)
	250	0.91(1)	2.87(2)	79(6)						
3	80	0.98(1)	3.27(3)	31(10)	0.98(1)	3.02(4)	35(11)	0.45(1)	0.60(1)	33(1)
	130	0.97(1)	3.18(3)	63(10)	0.96(1)	2.90(4)	19(10)	0.45(1)	0.62(2)	19(2)
	250	0.91(1)	2.88(2)	87(1)						
4	80	0.98(1)	3.23(3)	36(7)	0.99(1)	3.02(2)	33(8)	0.46(1)	0.55(1)	31(1)
	100	0.98(1)	3.18(1)	63(3)	0.98(1)	2.93(2)	18(3)	0.45(1)	0.54(2)	19(1)
	250	0.91(1)	2.83(2)	85(3)						

Fe_{HS}] complex arising from ferromagnetic coupling between two S = 2 centers, these percentages correspond to expected values of $\chi_M T$ = 3.49, 3.77, 4.61, and 7.69 cm^3 K mol^{-1} for **1**−**4**, respectively, which are close to the observed maximum values of $\chi_M T$ at low temperature. Although rudimentary, this analysis provides strong evidence that the incomplete spin crossover in **1**−**4** is best described as a conversion from [Fe_{HS}-Fe_{HS}] complexes at high temperature to a mixture of [Fe_{HS}-Fe_{HS}] and [Fe_{HS}-Fe_{LS}] complexes at low temperature, with the number of trapped [Fe_{HS}-Fe_{HS}] species increasing with increasing electron-withdrawing character of $^{X}L^{2-}$.

Mössbauer Spectroscopy. To further probe the spin crossover in **1**−**4**, zero-field Mössbauer spectra were collected for microcrystalline samples at selected temperatures. The Mössbauer spectra of all compounds at 250 K exhibit a major symmetric quadrupole doublet and a second minor doublet that is assigned to a small amount of Fe^{III}-containing impurity (Figure 5). Fits of the major doublet across the series gave an isomer shift of δ = 0.91(1) mm/s and a quadrupole splitting of ΔE_Q = 2.74(2)−2.88(2) mm/s (red lines in Figure 5), which is in good agreement with two high-spin Fe^{II} ions in a similar coordination environment.[53] We assign this doublet to the [Fe_{HS}-Fe_{HS}] species. As temperature was decreased to 150, 120, 130, and 100 K for **1**−**4**, respectively, this doublet developed shoulders. In addition, a new doublet with a much smaller quadrupole splitting appeared at lower velocity.

To further examine these spectral changes with decreasing temperature, the data for each compound were fit considering three distinct quadrupole doublets, two assigned to high-spin Fe^{II} ions and one assigned to low-spin Fe^{II}. This fit revealed that the doublet assigned to the high-spin Fe^{II} centers of the [Fe_{HS}-Fe_{HS}] species decreased considerably in intensity, now comprising only 21(20), 34(20), 63(10), and 63(3)% of the total spectrum for **1**−**4**, respectively, with slightly different parameters of δ = 0.96(1)−0.98(1) mm/s and ΔE_Q = 3.10(7)−3.24(5) mm/s (Table 4). This small increase in ΔE_Q with decreasing temperature is commonly observed for high-spin Fe^{II} centers and has been attributed to the increased population of low-lying excited states.[54] The fit also revealed the presence of an additional doublet corresponding to a second high-spin Fe^{II} center, with an isomer shift δ = 0.96(1)−0.98(1) mm/s and a quadrupole splitting of ΔE_Q = 2.89(13)−3.01(10) mm/s, along with relative areas of 44(27), 33(19), 19(10), and 18(3)% for **1**−**4**, respectively (green lines in Figure 5). Given the presence of two distinct high-spin Fe^{II} sites in each spectrum, we assign this second site to an [Fe_{HS}-Fe_{LS}] complex. This assignment is supported by previous reports wherein the two high-spin sites in a mixture of [Fe_{HS}-Fe_{HS}] and [Fe_{HS}-Fe_{LS}] complexes could be resolved by zero-field Mössbauer spectroscopy.[55] Here, the site with a smaller ΔE_Q was shown to correspond to the [Fe_{HS}-Fe_{LS}] complex, stemming from the distortion of the high-spin Fe^{II} coordination sphere imposed by spin crossover of the second Fe^{II} center.[55a,56] Finally, the third doublet, which accounts for 34(1), 33(2), 19(2), and 19(1)% of the spectra for **1**−**4**, respectively, exhibits parameters of δ = 0.44(1)−0.45(1) mm/s and ΔE_Q = 0.45(1)−0.62(2) mm/s (blue lines in Figure 5). These isomer shifts and quadrupole splittings are consistent with low-spin Fe^{II}, and as such we assign this site to the low-spin center of an [Fe_{HS}-Fe_{LS}] species.[56]

Upon further decreasing temperature to 80 K, we observed the continuation of this trend, revealing the additional decrease of the high-spin Fe^{II} site in [Fe_{HS}-Fe_{HS}] to 31(10) and 36(7)% for **3** and **4**, respectively, whereas both the high- and low-spin Fe^{II} sites in [Fe_{HS}-Fe_{LS}] increased to 33(1) and 35(11)% for **3** and 31(1) and 33(8)% for **4**, respectively. Moreover, in the cases of **1** and **2**, the data were best fit considering only two quadrupole doublets each, corresponding to the high- and low-spin centers of an [Fe_{HS}-Fe_{LS}] species, with no evidence for [Fe_{HS}-Fe_{HS}]. Indeed, this low-temperature behavior is consistent with that observed in magnetic measurements, which showed only a minor presence of [Fe_{HS}-Fe_{HS}] at low temperature. Taken together, this Mössbauer analysis further supports the hypothesis suggested by the magnetic measurements, which is that the spin crossover in **1**−**4** involves a mixed-spin [Fe_{HS}-Fe_{LS}] complex, with no evidence of an [Fe_{LS}-Fe_{LS}] species.

SUMMARY AND OUTLOOK

The foregoing results demonstrate that subtle, remote variation of the ligand field can lead to significant modulation of the crossover temperature in spin crossover Fe^{II}_2 complexes, as exemplified in complexes of the isostructural compounds $[(TPyA)_2Fe_2(^{X}L)]^{2+}$ (X = H, Br, Cl, and F). Indeed, the transition temperature ($T_{1/2}$) and enthalpy (ΔH) of spin crossover across this series were found to decrease from 160(1) to 110(1) K and from 11.4(3) to 7.5(2) kJ/mol in moving from X = H to F, respectively. While these parameters vary significantly with substituent, ΔS was found to remain relativity constant. This observation suggests that the trend is directly

dx.doi.org/10.1021/ic5025586 | Inorg. Chem. 2015, 54, 359−369

related to the associated change in enthalpy rather than entropy. Across the series, both $T_{1/2}$ and ΔH decrease with increasing electronegativity of X and consequently increasing electron-withdrawing character of $^{X}L^{2-}$, and both parameters scale linearly with the Pauling electronegativity of X. These trends suggest that the ligand field at Fe is dominated by contributions from inductive, rather than resonance, effects across the series. Finally, the low-temperature magnetic data, in conjunction with variable-temperature Mössbauer spectroscopy, suggest that the incomplete spin crossover behavior in $[(TPyA)_2Fe_2(^{X}L)]^{2+}$ is best described as a conversion from purely $[Fe_{HS}\text{-}Fe_{HS}]$ (HS = high-spin) complexes at high temperature to a mixture of $[Fe_{HS}\text{-}Fe_{HS}]$ and $[Fe_{HS}\text{-}Fe_{LS}]$ (LS = low-spin) complexes at low temperature, with the number of $[Fe_{HS}\text{-}Fe_{LS}]$ species increasing with decreasing electron-withdrawing character of $^{X}L^{2-}$. Future efforts will take advantage of the chemical tunability of $^{X}L^{2-}$ to increase $T_{1/2}$ by further modifying both electronic and steric properties of X. In addition, we will seek to engender magnetic bistability in related spin crossover compounds through replacement of $[BAr^{F}]^{-}$ with smaller counteranions in an effort to introduce large degrees of cooperativity.

■ ASSOCIATED CONTENT

Supporting Information

Crystal structures of **1′**, **2**, and **4′**, X-ray diffraction images of **1′**, additional magnetic data for **1**−**4**, and crystallographic information files (CIF) for **1′**, **2**, **3**, and **4′**. This material is available free of charge via the Internet at http://pubs.acs.org.

■ AUTHOR INFORMATION

Corresponding Author

*E-mail: dharris@northwestern.edu.

Author Contributions

†These authors contributed equally to this work.

Notes

The authors declare no competing financial interest.

■ ACKNOWLEDGMENTS

This research was funded by National Science Foundation Grant DMR-1351959, Northwestern University, the Chemistry of Life Processes Institute, and the International Institute for Nanotechnology. We thank J. A. DeGayner and J. Martinez for experimental assistance and Prof. J. M. Smith for helpful advice on the synthesis of $Fe(BAr^{F})_2\cdot 6MeCN$.

■ REFERENCES

(1) (a) Gütlich, P.; Goodwin, H. A. *Top. Curr. Chem.* **2004**, *233*, 1−47. (b) Halcrow, M. A. *Spin-Crossover Materials: Properties and Applications*; John Wiley and Sons, Ltd.: Oxford, U.K., 2013.

(2) Kahn, O.; Martinez, C. J. *Science* **1998**, *279*, 44−48.

(3) Létard, J.-F.; Guionneau, P.; Goux-Capes, L. *Top. Curr. Chem.* **2004**, *235*, 221−249.

(4) Bousseksou, A.; Molnár, G.; Demont, P.; Menegotto, J. *J. Mater. Chem.* **2003**, *13*, 2069−2071.

(5) (a) Muller, R. N.; van der Elst, L.; Laurent, S. *J. Am. Chem. Soc.* **2003**, *125*, 8405−8407. (b) Jeon, I-R.; Park, J. G.; Haney, C. R.; Harris, T. D. *Chem. Sci.* **2014**, *5*, 2461−2465.

(6) Halcrow, M. A. *Polyhedron* **2007**, *26*, 3523−3576.

(7) Gaspar, A. B.; Seredyuk, M.; Gütlich, P. *J. Mol. Struct.* **2009**, *9*, 924−926.

(8) Weber, B. *Coord. Chem. Rev.* **2009**, *253*, 2432−2449.

(9) Halcrow, M. A. *Chem. Soc. Rev.* **2011**, *40*, 4119−4142.

(10) Nakano, K.; Suemura, N.; Yoneda, K.; Kawata, S.; Kaizaki, S. *Dalton Trans.* **2005**, 740−743.

(11) Martínez, V.; Gaspar, A. B.; Muñoz, M. C.; Levchenko, G.; Real, J. A. *Chem.—Eur. J.* **2009**, *15*, 10960−10971.

(12) Rodríguez-Velamazán, J. A.; Carbonera, C.; Castro, M.; Palacios, E.; Létard, J.-F.; Burriel, R. *Chem.—Eur. J.* **2010**, *16*, 8785−8796.

(13) Lin, H.-J.; Siretanu, D.; Dickie, D. A.; Subedi, D.; Scepaniak, J. J.; Mitcov, D.; Clérac, R.; Smith, J. M. *J. Am. Chem. Soc.* **2014**, *136*, 13326−13332.

(14) Real, J. A.; Gaspar, A. B.; Muñoz, M. C.; Gütlich, P.; Ksenofotov, V.; Spiering, H. *Top. Curr. Chem.* **2004**, *233*, 167−193.

(15) Bousseksou, A.; Molnár, G.; Real, J. A.; Tanaka, K. *Coord. Chem. Rev.* **2007**, *251*, 1822−1833.

(16) Gaspar, A. B.; Muñoz, M. C.; Real, J. A. *J. Mater. Chem.* **2006**, *16*, 2522−2533.

(17) Olguín, J.; Brooker, S. Spin-Crossover in Discrete Polynuclear Complexes. In *Spin-Crossover Materials: Properties and Applications*; Halcrow, M. A., Ed.; John Wiley & Sons Ltd., Oxford, U.K., 2013; pp 77−120.

(18) Zein, S.; Borshch, S. A. *J. Am. Chem. Soc.* **2005**, *127*, 16197−16201.

(19) (a) Verat, A. Y.; Ould-Moussa, N.; Jeanneau, E.; Le Guennic, B.; Bousseksou, A.; Borshch, S. A.; Matouzenko, G. S. *Chem.—Eur. J.* **2009**, *15*, 10070−10082. (b) Matouzenko, G. S.; Jeanneau, E.; Verat, A. Y.; Bousseksou, A. *Dalton Trans.* **2011**, *40*, 9608−9618.

(20) Kitagawa, S.; Kawata, S. *Coord. Chem. Rev.* **2002**, *224*, 11−34.

(21) Miller, J. S.; Min, K. S. *Angew. Chem., Int. Ed.* **2009**, *48*, 262−272.

(22) Magnetic coupling measurements: (a) Pierpont, C. G.; Francesconi, L. C.; Hendrickson, D. N. *Inorg. Chem.* **1977**, *16*, 2367−2376. (b) Tinti, F.; Verdaguer, M.; Kahn, O.; Savariault, J.-M. *Inorg. Chem.* **1987**, *26*, 2380−2384. (c) Folgado, J. V.; Ibáñez, R.; Coronado, E.; Beltrán, D.; Savariault, J. M.; Galy, J. *Inorg. Chem.* **1988**, *27*, 19−26. (d) Chatterjee, P. B.; Bhattacharya, K.; Kundu, N.; Choi, K.-Y.; Clérac, R.; Chaudhury, M. *Inorg. Chem.* **2009**, *48*, 804−806. (e) Schweinfurth, D.; Klein, J.; Hohloch, S.; Dechert, S.; Demeshko, S.; Meyer, F.; Sarkar, B. *Dalton Trans.* **2013**, *42*, 6944−6952.

(23) Extended solids: (a) Nakabayashi, K.; Ohkoshi, S.-i. *Inorg. Chem.* **2009**, *48*, 8647−8649. (b) Abrahams, B. F.; Lu, K. D.; Moubaraki, B.; Murray, K. S.; Robson, R. *J. Chem. Soc., Dalton Trans.* **2000**, 1793−1797. (c) Nagayoshi, K.; Kabir, M. K.; Tobita, H.; Honda, K.; Kawahara, M.; Katada, M.; Adachi, K.; Nishikawa, H.; Ikemoto, I.; Kumagai, H.; Hosokoshi, Y.; Inoue, K.; Kitagawa, S.; Kawata, S. *J. Am. Chem. Soc.* **2003**, *125*, 221−232. (d) Luo, T.-T.; Liu, Y.-H.; Tsai, H.-L.; Su, C.-C.; Ueng, C.-H.; Lu, K.-L. *Eur. J. Inorg. Chem.* **2004**, 4253−4258. (e) Atzori, M.; Benmansour, S.; Espallargas, G. M.; Clemente-León, M.; Abhervé, A.; Gómez-Claramunt, P.; Coronado, E.; Artizzu, F.; Sessini, E.; Deplano, P.; Serpe, A.; Mercuri, M. L.; Gomez García, C. J. *Inorg. Chem.* **2013**, *52*, 10031−10040.

(24) Radical-bridged complexes: (a) Dei, A.; Gatteschi, D.; Pardi, L.; Russo, U. *Inorg. Chem.* **1991**, *30*, 2589−2594. (b) Min, K. S.; Rheingold, A. L.; DiPasquale, A.; Miller, J. S. *Inorg. Chem.* **2006**, *45*, 6135−6137. (c) Guo, D.; McCusker, J. K. *Inorg. Chem.* **2007**, *46*, 3257−3274. (d) Min, K. S.; DiPasquale, A. G.; Golen, J. A.; Rheingold, A. L.; Miller, J. S. *J. Am. Chem. Soc.* **2007**, *129*, 2360−2368. (e) Baum, A. E.; Lindeman, S. V.; Fiedler, A. T. *Chem. Commun. (Cambridge, U.K.)* **2013**, *49*, 6531−6533.

(25) Valence tautomerism: (a) Carbonera, C.; Dei, A.; Létard, J.-F.; Sangregorio, C.; Sorace, L. *Angew. Chem., Int. Ed.* **2004**, *43*, 3136−3138. (b) Tao, J.; Maruyama, H.; Sato, O. *J. Am. Chem. Soc.* **2006**, *128*, 1790−1791. (c) Li, B.; Tao, J.; Sun, H.-L.; Sato, O.; Huang, R.-B.; Zheng, L.-S. *Chem. Commun. (Cambridge, U.K.)* **2008**, 2269−2271. (d) Min, K. S.; DiPasquale, A. G.; Rheingold, A. L.; White, H. S.; Miller, J. S. *J. Am. Chem. Soc.* **2009**, *131*, 6229−6236.

(26) Spin crossover: (a) Min, K. S.; DiPasquale, A. G.; Rheingold, A. L.; Miller, J. S. *Inorg. Chem.* **2007**, *46*, 1048−1050. (b) Min, K. S.; Swierczek, K.; DiPasquale, A. G.; Rheingold, A. L.; Reiff, W. M.; Arif, A. M.; Miller, J. S. *Chem. Commun. (Cambridge, U.K.)* **2008**, 317−319.

(27) Tyeklár, Z.; Jacobson, R. R.; Wei, N.; Murthy, N. N.; Zubieta, J.; Karlin, K. D. *J. Am. Chem. Soc.* **1993**, *115*, 2677−2689.
(28) Mansell, S. M.; Perandones, B. F.; Arnold, P. L. *J. Organomet. Chem.* **2010**, *695*, 2814−2821.
(29) Bayen, S.; Barooah, N.; Sarma, R. J.; Sen, T. K.; Karmakar, A.; Baruah, J. B. *Dyes Pigm.* **2007**, *75*, 770−775.
(30) Nield, E.; Tatlow, J. C. *Tetrahedron* **1960**, *8*, 38−41.
(31) Mital, R. L.; Jain, S. K. *J. Chem. Soc. C* **1971**, 1875−1878.
(32) Reger, D. L.; Little, C. A.; Lamba, J. J. S.; Brown, K. J. *Inorg. Synth.* **2004**, *34*, 5−8.
(33) Cullinane, J.; Jolleys, A.; Mair, F. S. *Dalton Trans.* **2013**, *42*, 11971−11975.
(34) Syukri, S.; Radhakrishnan, N.; Herdtweck, E.; Voit, B.; Kühn, F. E. *Eur. J. Inorg. Chem.* **2008**, *18*, 2892−2898.
(35) *SAINT: Software for the Integration of CCD Detector System*, version 8.27B; Bruker AXS Inc.: Madison, WI, 2007.
(36) Sheldrick, G. M. *Acta Crystallogr., Sect. A: Found. Crystallogr.* **2008**, *64*, 112−122.
(37) Dolomanov, O. V.; Bourhis, L. J.; Gildea, R. J.; Howard, J. A. K.; Puschmann, H. *J. Appl. Crystallogr.* **2009**, *42*, 339−341.
(38) Bain, G. A.; Berry, J. F. *J. Chem. Educ.* **2008**, *85*, 532−536.
(39) (a) Das, H. S.; Weisser, F.; Schweinfurth, D.; Su, C.-Y.; Bogani, L.; Fiedler, J.; Sarkar, B. *Chem.—Eur. J.* **2010**, *16*, 2977−2981. (b) Sommer, M. G.; Schweinfurth, D.; Weisser, F.; Hohloch, S.; Sarkar, B. *Organometallics* **2013**, *32*, 2069−2078. (c) Das, H. S.; Schweinfurth, D.; Fiedler, J.; Khusniyarov, M. M.; Mobin, S. M.; Sarkar, B. *Chem.—Eur. J.* **2014**, *20*, 4334−4346.
(40) (a) Schweinfurth, D.; Khusniyarov, M. M.; Bubrin, D.; Hohloch, S.; Su, C.-Y.; Sarkar, B. *Inorg. Chem.* **2013**, *52*, 10332−10339. (b) Schweinfurth, D.; Rechkemmer, Y.; Hohloch, S.; Deibel, N.; Peremykin, I.; Fiedler, J.; Marx, R.; Neugebauer, P.; van Slageren, J.; Sarkar, B. *Chem.—Eur. J.* **2014**, *20*, 3475−3486.
(41) Zhang, D.; Jin, G.-X. *Organometallics* **2003**, *22*, 2851−2854.
(42) Jia, W.-G.; Han, Y.-F.; Lin, Y.-J.; Weng, L.-H.; Jin, G.-X. *Organometallics* **2009**, *28*, 3459−3464.
(43) (a) Kusz, J.; Gütlich, P.; Spiering, H. *Top. Curr. Chem.* **2004**, *234*, 129−153. (b) Lakhloufi, S.; Guionneau, P.; Lemée-Cailleau, M. H.; Rosa, P.; Létard, J.-F. *Phys. Rev. B* **2010**, *82*, 132104-1−132104-4. (c) Kusz, J.; Zubko, M.; Neder, R. B.; Gütlich, P. *Acta Crystallogr., Sect. B: Struct. Sci.* **2012**, *68*, 40−56.
(44) Guionneau, P.; Marchivie, M.; Bravic, G.; Létard, J.-F.; Chasseau, D. *Top. Curr. Chem.* **2004**, *234*, 97−128.
(45) Krüger, H.-J. *Coord. Chem. Rev.* **2009**, *253*, 2450−2459.
(46) Drew, M. G. B.; Harding, C. J.; McKee, V.; Morgan, G. G.; Nelson, J. *J. Chem. Soc., Chem. Commun.* **1995**, 1035−1038.
(47) (a) Ksenofontov, V.; Levchenko, G.; Spiering, H.; Gütlich, P.; Létard, J.-F.; Bouhedja, Y.; Kahn, O. *Chem. Phys. Lett.* **1998**, *294*, 545−553. (b) Stassen, A. F.; de Vos, M.; van Koningsbruggen, P. J.; Renz, F.; Ensling, J.; Kooijman, H.; Spek, A. L.; Haasnoot, J. G.; Gütlich, P.; Reedijk, J. *Eur. J. Inorg. Chem.* **2000**, 2231−2237. (c) Moliner, N.; Gaspar, A. B.; Muñoz, M. C.; Niel, V.; Cano, J.; Real, J. A. *Inorg. Chem.* **2001**, *40*, 3986−3991. (d) Stassen, A. F.; Grunert, M.; Dova, E.; Müller, M.; Weinberger, P.; Wiesinger, G.; Schenk, H.; Linert, W.; Haasnoot, J. G.; Reedijk, J. *Eur. J. Inorg. Chem.* **2003**, 2273−2282. (e) Money, V. A.; Carbonera, C.; Elhaïk, J.; Halcrow, M. A.; Howard, J. A. K.; Létard, J.-F. *Chem.—Eur. J.* **2007**, *13*, 5503−5514. (f) Létard, J.-F.; Asthana, S.; Shepherd, H. J.; Guionneau, P.; Goeta, A. E.; Suemura, N.; Ishikawa, R.; Kaizaki, S. *Chem.—Eur. J.* **2012**, *18*, 5924−5934. (g) Paradis, N.; Chastanet, G.; Varret, F.; Létard, J.-F. *Eur. J. Inorg. Chem.* **2013**, 968−974.
(48) Ksenofontov, V.; Gaspar, A. B.; Real, J. A.; Gültlich, P. *J. Phys. Chem. B* **2001**, *105*, 12266−12271.
(49) (a) Watt, K.; Baye, L. J.; Drummond, F. O., Jr. *J. Am. Chem. Soc.* **1966**, *88*, 1138−1140. (b) Atkins, P.; de Paula, J. *Physical Chemistry*, 8th ed.; Oxford University Press: Oxford, U.K., 2006; Chapter 5.
(50) The data were fit in the temperature range of 65−300 K.
(51) Gültlich, P.; Hauser, A.; Spiering, H. *Angew. Chem., Int. Ed.* **1994**, *33*, 2024−2054.
(52) Pauling, L. *J. Am. Chem. Soc.* **1932**, *54*, 3570−3582.
(53) Jeon, I-R.; Park, J. G.; Xiao, D. J.; Harris, T. D. *J. Am. Chem. Soc.* **2013**, *135*, 16845−16848.
(54) Merrithew, P. B.; Rasmussen, P. G.; Vencent, D. H. *Inorg. Chem.* **1971**, *10*, 1401−1406.
(55) (a) Ingalls, R. *Phys. Rev. A* **1964**, 787−795. (b) Grunert, C. M.; Reiman, S.; Spiering, H.; Kitchen, J. A.; Brooker, S.; Gültlich, P. *Angew. Chem., Int. Ed.* **2008**, *47*, 2997−2999. (c) Verat, A. Y.; Ould-Moussa, N.; Jeanneau, E.; Le Guennic, B.; Bousseksou, A.; Borshch, S. A.; Matouzenko, G. S. *Chem.—Eur. J.* **2009**, *15*, 10070−10082.
(56) Gütlich, P.; Bill, E.; Trautwein, A. X. *Mössbauer Spectroscopy and Transition Metal Chemistry: Fundamentals and Applications*; Springer-Verlag: Heidelberg, Germany, 2010.